Model-free control for an industrial long-stroke motion system with a nonlinear micropositioning actuator

Al-Rawashdeh, Yazan M.; Al Saaideh, Mohammad; Heertjes, Marcel F.; Oomen, Tom; Al Janaideh, Mohammad

DOI
10.1016/j.mechatronics.2024.103257

Publication date
2024

Document Version
Final published version

Published in
Mechatronics

Mechatronics 104 (2024) 103257

Contents lists available at ScienceDirect

Mechatronics

journal homepage: www.elsevier.com/locate/mechatronics

Model-free control for an industrial long-stroke motion system with a nonlinear micropositioning actuator☆

Yazan M. Al-Rawashdeh [a], Mohammad Al Saaideh [b], Marcel F. Heertjes [c,d], Tom Oomen [d,e], Mohammad Al Janaideh [f,*]

[a] Department of Electrical Engineering, Al-Zaytoonah University of Jordan, 130 Amman, 11733, Jordan
[b] Department of Electrical and Computer Engineering, Memorial University, St. John's, NL A1B 3X5, Canada
[c] ASML, Netherlands
[d] Department of Mechanical Engineering at Eindhoven University of Technology, 5612 AZ Eindhoven, Netherlands
[e] Department of Mechanical Engineering at Delft University of Technology (TU Delft), 2628 CD Delft, Netherlands
[f] School of Engineering, University of Guelph, Guelph, ON N1G 2W1, Canada

ARTICLE INFO

Keywords:
Wafer scanner
Dual-stage motion system
Piezoelectric actuator
Model-free control
Active-inhibit trajectory generator

ABSTRACT

Fine positioning stages based on piezoceramic materials have found widespread success in various applications due to their attractive features. However, the inherent hard nonlinear behavior of piezoelectric actuators complicates modeling, control, and synchronization processes. In this study, adopting an input–output perspective, we propose and experimentally verify a model-free control and synchronization technique for these stages. Specifically, our approach introduces a model-free trajectory generator that adjusts the desired trajectory using position measurement data to minimize tracking errors. We validate this technique using a representative precision motion system, consisting of a planner stage and a uni-axial fine stage, under step-and-scan trajectories commonly employed in wafer scanners. Remarkably, despite its simplicity, the proposed design procedure can be seamlessly extended to other robotics and automation applications.

1. Introduction

When aiming for nanometer precision accuracy in motion system design, an effective strategy involves integrating coarse and fine positioning stages that complement each other in precision and tracking capabilities [1]. In a dual-stage motion system, the long-stroke (LS) stage handles extensive distances in the meter range, while its counterpart, the short-stroke (SS) stage, operates within the micro-meter range, creating a dynamic synergy [2–4]. Dual-stage motion system finds widespread application with nano-precision movements, particularly in critical sectors like robotics applications [5], micromachining [6–8], and wafer scanners in semiconductor manufacturing [9]. Industries like semiconductor manufacturing [10] have also embraced this setup. Consider, for instance, producing nanometric integrated circuits (ICs) utilizing wafer scanner machines. In this process, replicas of IC images are projected onto a light-sensitive silicon disk, known as a wafer, using quartz plate masks [9,11]. This intricate LS-SS orchestration plays a crucial role in achieving the precision demanded by such applications, showcasing the adaptability and efficacy of this motion system configuration. In essence, step-and-scan motion trajectories take center stage in scanning small rectangular areas, referred to as dies, on the wafer during the scanning process. The transition between dies is accomplished through a stepping process, as detailed in [12]. In the stepping phase, speed is optimized under high acceleration motion profiles, whereas scanning is executed at a predetermined constant velocity. However, the challenge arises in maintaining precision at these high acceleration rates, necessitating the incorporation of additional stages [9]. Introducing more stages, though, comes with the trade-off of increased weight. As a solution, the quest for next-generation wafer scanners involves integrating lightweight stages capable of swift and accurate actuation. Notably, the contemporary trend leans towards the adoption of piezoelectric actuators, commonly known as piezo actuators, to drive flexure-guided piezo stages in the short-stroke (SS) domain, marking a rising preference in recent developments [4,13,14]. This strategic shift showcases the industry's pursuit of speed and precision in the ever-evolving landscape of wafer scanning technology.

Complementary short-stroke fine positioning stages are usually introduced to enhance the precision of coarse long-stroke motion axes.

☆ This paper was recommended for publication by Associate Editor Oliver Sawodny.

* Corresponding author.
E-mail addresses: y.alrawashdeh@zuj.edu.jo (Y.M. Al-Rawashdeh), mialsaaideh@mun.ca (M. Al Saaideh), marcel.heertjes@asml.com (M.F. Heertjes), t.a.e.oomen@tue.nl (T. Oomen), maljanai@uoguelph.ca (M. Al Janaideh).

https://doi.org/10.1016/j.mechatronics.2024.103257
Received 22 May 2024; Received in revised form 23 July 2024; Accepted 20 September 2024
Available online 9 October 2024

For example, the long-stroke stage achieves a millimeter range of motion with micrometer precision, while the short-stroke achieves a micrometer range of motion with nanometer precision. Combining both types of motion results in a millimeter range of motion with nanometer precision thanks to the quick response of the short-stroke stage compared to the long-stroke stage whose tracking error can be compensated while in motion according to the herein proposed approach. As these stages are mechanically attached, controlling and synchronizing their motion becomes necessary.

Suitable model-based controllers for fine stages are typically designed based on sophisticated models and identification techniques. Integrating piezoelectric actuators in dual-stage motion systems ensures nanometer-level precision and enables swift and accurate adjustments. Recently, they have found use in high-acceleration motion scenarios such as wafer scanners, where high precision is vital despite the involvement of significant inertial forces. The long-stroke stage provides the necessary reach and macro-scale motion, while the short-stroke stage complements the overall system dynamics with finer control and micro-scale precision. The short-stroke stage driven by piezoelectric actuators stands at the forefront of achieving intricate positioning tasks with unparalleled accuracy and efficiency in diverse applications such as wafer scanners in semiconductor manufacturing [1,4,15,16]. While piezoelectric actuators offer remarkable precision and responsiveness in dual-stage motion systems, they have drawbacks. The piezoelectric actuator exhibits inherent non-linear behaviors, such as hysteresis, creep, thermal drift, and vibrations, which collectively degrade the overall performance of dual-stage motion systems, including positioning accuracy and repeatability [17,18]. Balancing the advantages and drawbacks of piezoelectric actuators is crucial when considering their implementation in dual-stage motion systems, especially in applications demanding both precision and accuracy. The control system significantly influences the overall dynamics, encompassing positioning and tracking objectives, in a dual-stage motion system utilizing piezoelectric actuators [18]. From a control standpoint, various methods, including mixed compliance compensation [4], inversion-based feedforward control [19], adaptive feedforward/feedback combined controller [20], and iterative learning control [21], are employed to govern the dynamics of a piezo actuator. However, despite its notable advantages, the piezo actuator is not without its challenges, contending with creep, vibration, and hysteresis effects that demand effective compensation strategies [4]. Employing model-based control techniques involves utilizing apt models capable of capturing the nonlinear behaviors inherent in nanopositioning actuators. Examples of such models include the Rate-dependent Prandtl–Ishlinskii (RDPI) hysteresis model [22,23], the Memory-Element-Based Hysteresis model [24,25], the highly non-linear generalized Bouc-Wen mode [26] and the Dahl model-based hysteresis compensation [27], which adopts a system structure described by the Hammerstein system. This system structure comprises a linear dynamics subsystem flanked by input and output (hard) nonlinearities [28]. While model parameters are identified in this process [28], accurately pinpointing their values remains a challenging task [29]. This challenge becomes a potential roadblock in achieving seamless synchronization between the long-stroke (LS) and short-stroke (SS) motions, where the LS tracking error is typically fed, as is, to the SS controller [4]. Inversion-based feedforward controllers emerge as crucial elements in motion systems [30], where the inverse of the driven motion dynamics is acquired whenever possible. This inverse is then harnessed to design a stable feedforward system primarily processing predefined and supplied trajectory signals [30,31]. Meanwhile, to address disturbance rejection, the incorporation of feedback controllers becomes imperative [9]. This dual approach ensures the attainment of acceptable levels of system robustness and disturbance rejection capabilities, showcasing the intricate dance between model-based precision and the practicalities of real-world control systems.

Model-free techniques can also be used when exact models cannot be obtained. For example, in [32], an ultra-local representation for a three-axis coupled nanopositioning piezoelectric actuated platform is proposed and used to design a model-free adaptive proportional-integral controller that handles the actuation coupling effects and the hysteresis. Strain gauge sensors are used to provide position measurements of the platform, where some of the involved parameters are estimated using numerical differentiation or observers. In [33], an input–output data-driven, i.e., model-free, sliding mode controller that controls piezoelectric actuators suffering from time delay is presented. The resulting control loop can handle external disturbances and uncertainties. In [34], a robust tracking of force is achieved using a simple and model-free proportional-derivative controller that handles nonlinearities, external uncertainties and disturbances in a computationally efficient way such that safe human–robot interaction is guaranteed. The involved time delay is estimated. The resulting system is utilized to actively enable variable damping and to ensure physical compliance of the mechanism actuated using piezoelectric actuators. The time variation in the measured force is obtained using numerical differentiation and suitable low-pass filters. Similar to [32,33], in this study we propose a model-free technique that handles existing nonlinearities, uncertainties and external disturbances found in nanopositioning piezoelectric actuated platforms (stages). As in [32,34], we utilize numerical differentiation and suitable low-pass filters to obtain some of the needed signals where position measurements are assumed available. While [33,34] can handle available time delays, the herein proposed technique is not tested under such conditions. Moreover, in [32–34] robust model-free tracking controllers are developed, while in this study a simple yet robust input–output data-based model-free trajectory generator that acts as an input shaper is developed. Despite its applicability in various robotic applications, the performance of the developed trajectory generator is validated using a uni-axial piezoelectric actuated stage targeting mainly semiconductor manufacturing.

The main contribution includes the following:

- Adopting an input–output perspective, we propose the activator-inhibitor trajectory generator as a model-free input shaper based on output measurements to control the fine positioning stages actuated by piezoceramic actuators.
- Integrating the long-stroke (LS) of an existing precision motion system with the piezoactuated short-stroke (SS) stage to construct a dual-stage positioning system holds the promise of delivering superior sub-nanometer accuracy,
- Proposing a model-free active-inhibit trajectory generator that modifies the desired trajectories such that the tracking performance of the piezo-actuated SS is enhanced, and
- Combining LS and SS stages results in enhancing the scanning performance of the dual-stage system under a particular step-and-scan trajectory used mainly in wafer scanners. The overall performance will be compared to the model-based RDPI technique.

The remainder of the paper is summarized as follows, Section 2 includes the system description and the specifications of the long-stroke and short-stroke stages and their interaction. Moreover, the modeling of the short-stroke stage is formulated in this section using one model-based technique to facilitate comparison with the herein-proposed technique. Section 3 presents the mathematical formulation of the proposed model-free trajectory generator. Then, the experimental testing, validation, and comparison of the short-stroke stage performance using the proposed trajectory generator and the model-based RDPI method under different operating conditions are presented in Section 4. As an industrial application, the integration of the short-stroke and the long-stroke stages as a dual-stage motion system is presented in Section 5. Finally, Section 6 concludes the paper and proposes future work.

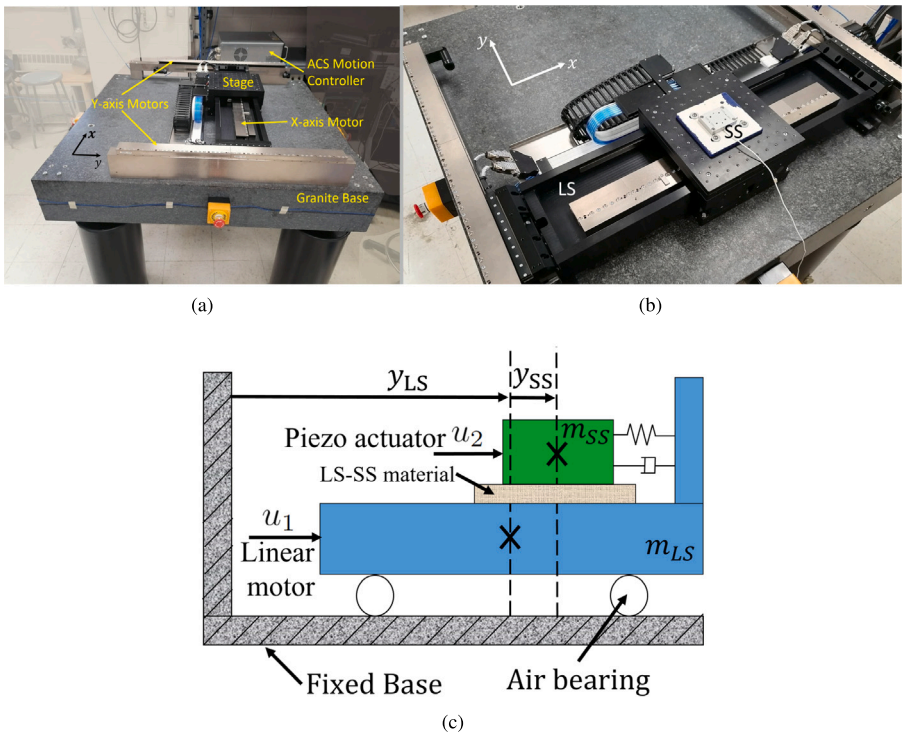

Fig. 1. (a) The dual-stage motion system considered in this study, (b) the used long-stroke LS, and the short-stroke SS aligned in the x-direction, and (c) a simplified model of LS-SS mechanical and electromagnetic uni-directional interactions along the y-axis.

2. System description

The proposed dual-stage motion system considered in this study has an integration of a Long-stroke (LS) stage and a Short-stroke (SS) stage, as shown in Fig. 1.

2.1. Long-stroke stage

The LS stage depicted in Fig. 1(a) is the A-322 PIglide HS XY Planar Scanner from PI (Physik Instrumente) L.P. This system boasts a resolution of 1 nm and includes the A-824 ACS Motion Controller, which operates at a default cycle time of 0.5 ms and a frequency of 400 Hz. It features three ironless, zero-cogging, brushless 3-phase linear motors arranged in an H-configuration [35], along with an air bearing levitation system. The entire setup is configured in a gantry design and supported by a passive anti-vibration system from Thorlabs. The feedback loop utilizes absolute encoders for position feedback, with velocity and acceleration derived internally through appropriate filters.

2.2. Short-stroke stage

The short-stroke stage depicted in Fig. 1(b) is a nanopositioning stage driven by a piezoelectric actuator. Specifically, it is the Nano-OP30 uni-axial nanopositioning stage from MAD City Lab Inc., offering a motion range of 30 µm. This stage features internal positioning powered by the innovative PicoQ technology, capable of delivering absolute and repeatable position measurements with a resolution of 0.06 nm. It is driven by a Nano-Drive amplifier, which provides high-voltage up to 150 V and collects position measurements. The Nano-Drive has an analog input range of ±10 V and an analog output range of $[0, 10]$ V.

2.3. Combining long-stroke and short-stroke stages

Referring to Fig. 1(c), when the SS (piezo-actuated) stage is mechanically attached to the LS stage, it shares the motion kinematics of m_{LS} as detailed in [35]. The SS stage will be mounted on the x-axis of the LS stage and can be aligned with either the x or y axis. For step-and-scan profiles, the SS stage is aligned with the LS y-axis, which is the scanning direction. It is important to note that during the modeling, identification, and controller design steps, the SS stage is handled independently from the LS stage, with no interactions between the two.

2.4. Short-stroke stage modeling

In general, the SS stage can be modeled as the Hammerstein system (Σ_1) depicted in Fig. 2, where the unknown dynamics is given as a cascade connection of an input hysteresis nonlinearity $\mathcal{M}$ that usually limits the system performance [28] and a linear dynamical part G_p, which presents the damping ratio and natural frequency of the system. Interestingly, Σ_1 presents the dynamic model of the SS stage with an input signal $r(t)$, an output position $p_a(t)$ and subjected to an external unknown disturbance $d(t)$. The main control objective of the SS stage, it is intended to minimize the tracking error $(e(t) = p_d(t) - p_a(t))$ between the desired position $p_d(t)$ and the actual system response $p_a(t)$. The most popular control approach for the piezo-actuated stage is using a feedforward (FF) compensation based on the inverse model of Σ_1, where the FF controller act as an internal model controller that inverts the Hammerstein system under the desired command intern see for example [22,22,23]. Clearly, when $d(t) \neq 0$, the performance under only the FF controller will deteriorate, and as a remedy, closed-loop controllers can be used instead, such as retrospective cost adaptive control (RCAC) [36] especially when $d(t)$ is unknown.

In that case, model-based control techniques require and estimation of Σ_1 dynamics, which might be limited due to the availability of the measurements in the system. Therefore, this study investigates a model-free control technique using the available measurements of the system. Note that $p_d(t)$ along with any needed ith time derivative $(p_d^{(i)})$ are externally supplied, $u(t)$ is designed, $v(t)$ are inaccessible, i.e., unknown intermediate signals [28,37], $d(t)$ is unknown, and $p_a(t)$ is assumed to be observable along with any needed ith time derivative

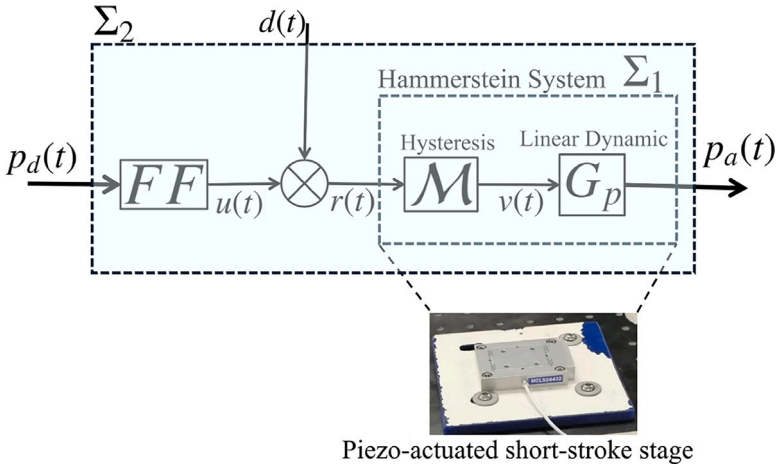

Fig. 2. Hammerstein system Σ_1 with unknown input nonlinearities, subjected to external disturbance $d(t)$, and the system Σ_2 presents the system Σ_1 under the feedforward controller FF with desired position $p_d(t)$ and output position $p_a(t)$.

$(p_a^{(i)})$ being readily available for measurements or can be estimated using model-free observers [38,39].

2.5. Industrial application

Among the possible applications that can be addressed by this study, wafer scanners play a significant role in semiconductor manufacturing. To increase their throughput while maintaining the performance, dual-stroke motion systems are usually used where a combination of a coarse long-stroke (LS) with sub-micro precision, and a fine short-stroke (SS) with possibly sub-nano precision [9] is utilized. In this LS-SS configuration, the tracking error of LS (e_{LS}) is fed into the SS to reduce the overall tracking error that happens to be equal to the SS tracking error (e_{SS}). To meet the requirements of next-generation wafer scanners, the use of piezoceramic actuated positioning stages as SS is recently being investigated [4]. Additionally, since the dynamics of piezoceramic actuated systems can be captured using Σ_1 depicted in Fig. 2 [40] with possibly only input hysteresis [36], such system will be the main focus of this study. Note that the herein proposed technique was used to enhance the performance of linear flexible motion system, simply because it requires very little-if any at all—information about the driven motion system, i.e., it is model-free. In this paper, the FF controller is realized as a simple static-gain controller to clearly reveal the attainable performance boost under the proposed activate-inhibit technique.

3. Model-free trajectory generation system

Adopting input–output perspective from $p_d(t)$ to $p_a(t)$ yields the system Σ_2 depicted in Fig. 2. The proposed control approach mainly involves a trajectory generator system (Σ_3) shown in Fig. 3, which produces a modified version of $p_d(t)$, denoted as $(\hat{p}_d(t))$, instead of adjusting $u(t)$ directly. This method aims to minimizing the tracking error $e(t) = p_d(t) - p_a(t)$, as will be demonstrated here. Consequently, maintaining or enhancing the performance of Σ_2 under FF—or other used control techniques-when $d(t) \neq 0$ and/or Σ_1 dynamics are unknown is made possible. This means that any existing control loops are kept intact as long as Σ_2 is input-to-state stable [41]. The proposed trajectory generation is a model-free technique since it does not require any knowledge about the systems Σ_1 or Σ_2. It is formulated based on the available measured position $p_a(t)$ or its derivatives.

The interaction between Inhibitor (Σ_2) and Activator (Σ_3) systems is depicted in Fig. 3.

3.1. Error estimates

Let $p_d^{(i)} = q_{i+1}$, and $p_a^{(i)} = x_{i+1}$ with $i = 0, 1, \dots, n$ with $n \geq 1$. To make Σ_3 aware of Σ_2 tracking error $e = q_1 - x_1$, let the dynamics of the tracking error estimates $(\hat{e}_i)$ be given according to the following state estimator (observer)

$$\dot{\hat{e}}_i = \hat{e}_{i+1} + \beta_i \left(x_1 - q_1\right), \; i = 1, 2, \dots, n-1 \tag{1}$$

$$\dot{\hat{e}}_n = \hat{\sigma} + \beta_n \left(x_1 - q_1\right) + \beta_0 \left(x_{n+1} - q_{n+1}\right) \tag{2}$$

$$\dot{\hat{\sigma}} = \beta_{n+1} \left(x_1 - q_1\right) \tag{3}$$

with constants $\beta_i > 0 \in \mathbb{R}, i = 0, 1, \dots, n+1$ are chosen such that $(1+\beta_0)\, s^{n+1} + \beta_1\, s^n + \beta_2\, s^{n-1} + \cdots + \beta_{n+1} = 0$ is Hurwitz, where β_0 is chosen to reflect the dependency on the available measurements (or estimates) of Σ_1. For example, when acceleration measurements are available, $1 \leq n \leq 2$ can be used in (3) under which Σ_3 will activate Σ_2 using the modified desired input $(\hat{p}_d)$, and Σ_2 will inhibit Σ_3 using $\hat{e}_1$ in an activator-inhibitor interaction.

Ultimately, it is desired to reduce the tracking error $e_1 = p_d - x_1$ by re-adjusting p_d such that $\mathbf{x} = \left[x_1, x_2, \dots, x_{n+1}\right]^{\mathrm{T}}$ meets any imposed motion requirements. Let $\mathbf{q} = \left[q_1, q_2, \dots, q_{n+1}\right]^{\mathrm{T}}$, and $\hat{\mathbf{q}} = \left[\hat{q}_1, \hat{q}_2, \dots, \hat{q}_{n+1}\right]^{\mathrm{T}}$ with $\hat{q}_1$ be given as

$$\hat{p}_d(t) \equiv \hat{q}_1 = q_1(t) - \hat{e}_1(t) \tag{4}$$

and other modified kinematical quantities given as

$$\hat{q}_i = q_i(t) - \hat{e}_i(t), \; i = 2, \dots, n+1 \tag{5}$$

Therefore, in the frequency domain and using the Laplace operator (s) with zero initial conditions, (3) is given as

$$\begin{aligned} \hat{e}_1 &= \frac{(\beta_0\, s^{n+1} + \beta_1\, s^n + \beta_2\, s^{n-1} + \cdots + \beta_{n+1})\,(x_1 - \hat{q}_1)}{(1+\beta_0)\, s^{n+1} + \beta_1\, s^n + \beta_2\, s^{n-1} + \cdots + \beta_{n+1}} \\ &= G_e(s)\,(x_1 - \hat{q}_1) \end{aligned} \tag{6}$$

Using (4) in (6), yields

$$x_1 = q_1 + \left\{ \frac{1 - G_e(s)}{G_e(s)} \right\} \hat{e}_1 \tag{7}$$

Consequently, the constants $\beta_i > 0$ should be chosen such that Σ_3 is stable, and $\|G_e(j\,\omega)\|_\infty$ is *ideally* close to unity $\forall\omega$ in the frequency domain of interest. Doing so results in $x_1 = q_1$ as required. Interestingly, when β_i in (3) is taken as $\beta_i = \gamma_i/\epsilon^{(i)}$ with $1 \gg \epsilon > 0, \gamma_i > 0 \in \mathbb{R}$ and $\epsilon^{(i)}$ denotes ϵ to the ith power, then the link with high-gain observers is established where an estimate of the tracking error $e_1 = p_d - p_a$ under open-loop configuration can be used to adjust the desired input as given by (4) under activator-inhibitor configuration [42]. Moreover,

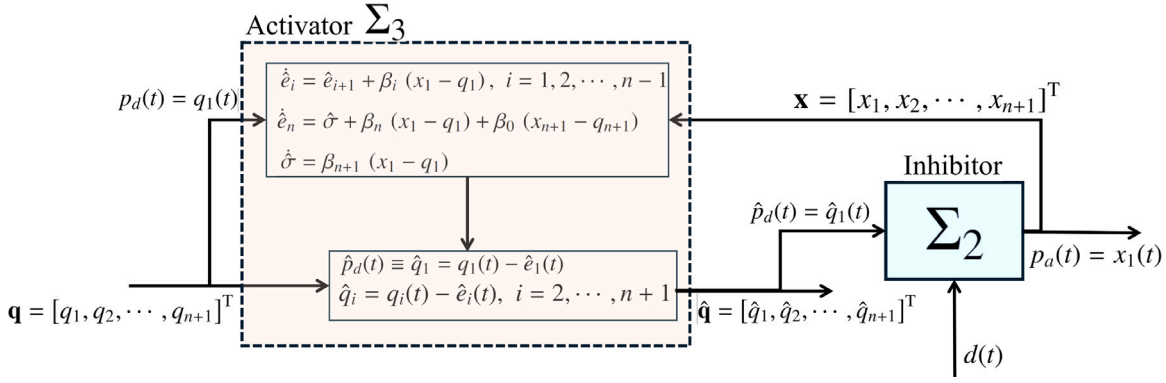

Fig. 3. Block diagram representations of the controlled Hammerstein system under $\Sigma_3 \leftrightarrow \Sigma_2$ interaction.

(3) seems to be linked to RCAC [36], with the exception that the former can be easily designed off-line, especially when the operating frequency range of the desired position signal $p_d(t)$ is predictable as can be found in repetitive motion profiles found in wafer scanners [43], for example. Comparing both techniques is beyond the scope of this investigation.

According to lemma 4.7 in [44] and assuming Σ_2 to be input-to-state stable under the used control technique, and the origin of Σ_3 is globally uniformly asymptotically stable, then the origin of the cascaded system Σ_2 and Σ_3 is globally uniformly asymptotically stable.

3.2. Desired motion profiles

Consider the generalized fillet motion profile depicted in Fig. 4, which can be used to design the desired signal ($\boldsymbol{p}$) as the step-and-scan trajectory meant for wafer scanners, i.e. step along x-axis, and scan along the y-axis. Using third-order polynomials with switched coefficients:

$$\boldsymbol{p}(t) := \begin{cases} x_d\ (t_x) = \alpha_0^k + \alpha_1^k\, t_x + \alpha_2^k\, t_x^2 + \alpha_3^k\, t_x^3 \\ y_d\ (t_y) = \beta_0^q + \beta_1^q\, t_y + \beta_2^q\, t_y^2 + \beta_3^q\, t_y^3, \end{cases} \tag{8}$$

with $t_{\{x,y\}} = \left(t - t_{0_{\{x,y\}}}\right)$, $t_{0_{\{x,y\}}}$ denotes the trajectory time shift in the x, y motion, and the switched coefficients α_l^k, β_l^q with $l = 0, 1, 2, 3$ in the k, q intervals are symbolically given in [45]. These switched coefficients are functions of the maximum acceleration value ($a^{max}_{\{step,scan\}}$) given in m/s^2, the time interval of acceleration and deceleration (T_1), the interval of constant acceleration (T_2), the constant speed intervals ($D, d \equiv T_w$) all given in s, and the scaling factors ($s_{\{step,scan\}} > 0$) that are taken here as 1 and thus absent in the current formulation.

The step-and-scan trajectory can be characterized by several key features–as discussed in [45,46]–among which the scanning phase pitch size (P_{scan}), and the constant scanning speed (V_{scan}) given as [45]

$$P_{scan} = V_{scan}\ (2\,T_1 + T_2 + D) \tag{9}$$

$$V_{scan} = a^{max}_{scan}\ (T_1 + T_2), \tag{10}$$

also the stepping phase pitch size (P_{step}) given as [45]

$$P_{step} = a^{max}_{step}\ (T_1 + T_2)\ (2\,T_1 + T_2 + d) \tag{11}$$

Consider the step-and-scan motion of 10 dies as shown in Fig. 5, where $P_{scan} = 0.0623125$ m, $P_{step} = 0.026$ m, $T_1 = 0.04285$ s, $T_2 = 0.040476$ s, $D = 0.123059$ s, $d \equiv T_w = 0.020$ s, $a^{max}_{step} = 2.14285$ m/s^2, and $a^{max}_{scan} = 3$ m/s^2. Using these values, the tracking error of the LS stage (e_{LS}) under the realized fillet profile can be obtained. Its frequency contents will be instrumental when (6) is designed, as will be discussed shortly.

4. Experimental testing and validation of the short-stroke stage

A uni-axial piezoelectric-actuated Nano-OP30 stage is used to realize a nanopositioning SS motion system with a motion range of 30 μm. This stage has only a position sensor with a resolution of 0.06 nm that provides clean measurements of $p_a(t)$, and therefore, any needed $p_a^{(i)}$ is obtained using numerical differentiation, i.e., no states estimation is required, and signal filtering. In this study, Butterworth filters are used to maintain an adequate quality of $p_a^{(i)}$. The FF controller used in Σ_2 is a static gain, i.e., 1/1.5045 (V/μm). Knowing the desired position signal $p_d(t)$ operating frequency, $G_e(s)$ in (6) can be designed, and its bandwidth (BW$\{G_e(s)\}$) can be assigned. According to Fig. 2, e_{LS} can serve as the input to Σ_2, i.e., $p_d(t) \equiv e_{\mathrm{LS}}(t)$, in an LS-SS configuration. However, in this section, harmonic command inputs will be utilized with any desired $p_d^{(i)}$ being available. Consider the test input signal given as

$$p_d(t) = \sum_{i=1}^{m} A_i\ \cos\left(\omega_i\, t + \alpha_i\right) \tag{12}$$

where $m >= 1$ denotes the test signals involved each with frequency $\omega_i \in \mathrm{BW}(G_e(s))$, and amplitudes $A_i \in \mathbb{R}$ such that $\max\{|p_d(t)|\} \le d_{\max}$ with $d_{\max}$ denotes the maximum displacement, i.e., ±15 μm, and α_i are the phase shift angles used. Using the acceleration measurements with $n = 2$ in (6) results in $G_{e_a}(s)$, and using the velocity measurements with $n = 1$ results in $G_{e_v}(s)$, where both are given as

$$G_{e_a}(s) = \frac{0.002\,s^3 + 520\,s^2 + 0.3\,s + 2}{1.002\,s^3 + 520\,s^2 + 0.3\,s + 2} \tag{13}$$

$$G_{e_v}(s) = \frac{0.05\,s^2 + 425\,s + 100}{1.05\,s^2 + 425\,s + 100} \tag{14}$$

and their frequency response function and Bode plots are depicted in Fig. 6. Note that when $\mathrm{BW}\{G_{e_a}(s)\} \approx \mathrm{BW}\{G_{e_v}(s)\}$, the performance of Σ_3 realized using G_{e_a} deteriorates more compared to the one realized using G_{e_v} outside the designated bandwidth. This may suggest the superiority of using lower values of n provided that the desired bandwidth can be achieved using the available number of coefficients, such that $|G_e(s)| = 0$ dB and $\angle G_e(s) = 0$.

4.1. Testing without disturbances $d(t) = 0$

Using (12) and $G_{e_a}(s)$ with $d(t) = 0$, the performance of $\Sigma_3 \leftrightarrow \Sigma_2$ interaction according to Fig. 3 is assessed. Starting with a single frequency test signal, i.e., $m = 1$, with $\alpha_1 = -0.5\pi, A_1 = 5$ μm, and $\omega_1 = 2\pi f_1 t$ where $f_1 \in \{5, 15\}$ Hz $\in \mathrm{BW}\{G_{e_a}(s)\}$, the time responses of the $\Sigma_3 \leftrightarrow \Sigma_2$ signals $p_a(t), e(t) = p_d(t) - p_a(t)$ are depicted in Fig. 7. Similar to the attainable BW$\{G_e(s)\}$, the transient responses of $p_a(t), e(t)$ signals are dictated by the β_i constants used. Designing a tuning algorithm that ensures generating dynamically friendly modified trajectories will be investigated in future work. The input–output

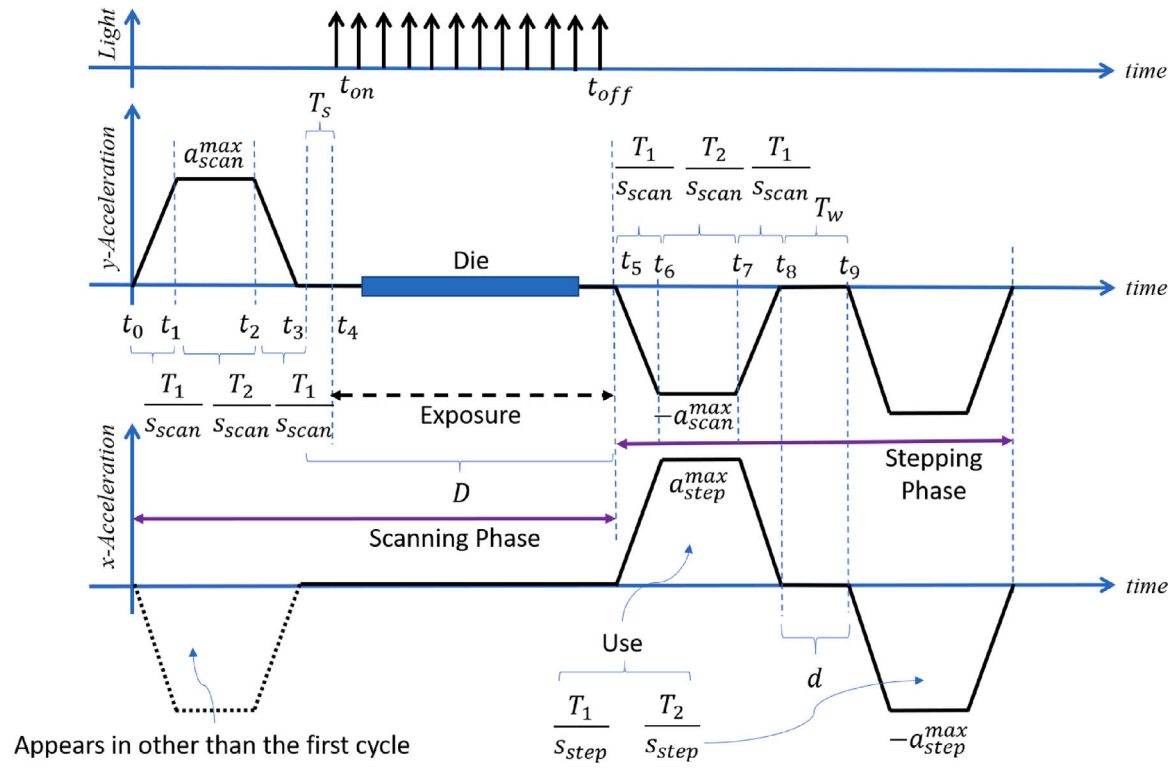

Fig. 4. Fillet acceleration trajectories along with the light source activation timing, resulting in a step-and-scan motion of one die [45].

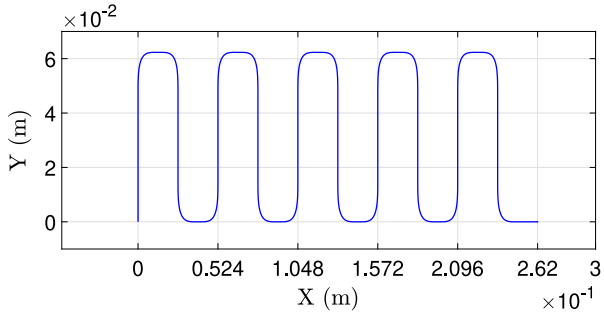

Fig. 5. A Step-and-scan motion profile of 10 dies.

characteristic of $\Sigma_3 \leftrightarrow \Sigma_2$ interaction is depicted in Fig. 8, where Σ_3 inverts Σ_2 at the frequency of the test signal. Having $p_d(t) = 5\sin(2\pi f t)$ with $f \in \{5, 10, 15, 20\}$ Hz, $G_{e_a}(s)$, and $G_{e_v}(s)$, the performance under $\Sigma_3 \leftrightarrow \Sigma_2$ interaction is summarized in Table 1, where $G_{e_a}(s)$, and $G_{e_v}(s)$ resulted in almost an identical performance in the mean-square error (MSE) sense. Note that $f = 20$ Hz is slightly outside BW$\{G_{e_a}(s)\}$, which justifies the performance drop at that frequency. Now, using (12), $m = 4$, $G_{e_v}(s)$, and $d(t) = 0$, a mixed-frequency test input signal is realized as $p_d(t) = A_1 \sin(20\pi t + 1.5\pi) + A_2 \cos(30\pi t) + A_3 \sin(40\pi t + 1.5\pi) + A_4 \cos(60\pi t)$ with $A_1 = 0.75, A_2 = 2.25, A_3 = 1.5, A_4 = 1.05$, where Fig. 9 shows the resulting Σ_3 performance and its compensation. Using the previous $p_d(t)$ signal with $A_1 = 1.75, A_2 = 5.25, A_3 = 3.5, A_4 = 2.45$, Σ_3 retains its performance over a larger range of motion while having frequencies outside BW$\{G_{e_v}(s)\}$, as shown in Fig. 10.

4.2. Robustness of the activate-inhibit trajectory generation

This section aims to test and validate the robustness of the activate-inhibit trajectory generation for the short-stroke stage subjected to unknown load mass m_l variation and unknown external disturbances $d(t)$ during motion. Consider the tracking error depicted in Fig. 11 where a load mass of 0.5 kg is added while the stage is in motion. Clearly, the proposed techniques are capable of handling such a variation in the load mass.

Table 1
Comparison of $\Sigma_3 \leftrightarrow \Sigma_2$ and Σ_2 control scheme with $p_d(t) = 5\sin(2\pi f t)$ µm.

f (Hz)	MSE $\{e_1(t)\}$ (µm)			Max $\{\lvert e_1(t)\rvert\}$ (µm)		
	$\Sigma_3 \leftrightarrow \Sigma_2$		Σ_2	$\Sigma_3 \leftrightarrow \Sigma_2$		Σ_2
	G_{e_a}	G_{e_v}		G_{e_a}	G_{e_v}	
5	0.0018	0.0009	0.1282	0.1638	0.1275	0.5913
10	0.0100	0.0112	0.4913	0.2940	0.2618	1.1119
15	0.0562	0.0602	1.0988	0.6057	0.5113	1.6191
20	0.1513	0.1945	1.9416	0.9028	0.7806	2.1927

Recalling Fig. 2, the disturbance $d(t) \neq 0$ V is realized using two unit-step inputs and a harmonic signal $0.5\sin(50\pi t)$ with frequency outside the bandwidth of $G_{e_v}(s)$ given in (14)—as depicted in Fig. 12. According to Fig. 13, Σ_3 successfully rejected the active disturbance while maintaining the tracking performance. The mechanism by which Σ_3 can reject the disturbance manifests itself in the modified desired trajectories, $\hat{p}_d(t)$ as can be seen from Fig. 14.

4.3. Reference signals and disturbances with higher-frequencies

To show the ability of the proposed approach to handle reference signals with higher operating frequencies, the involved parameters given in (14) can be re-tuned to extend the bandwidth of the resulting activator system. For example, compare the tracking errors of a reference signal $p_d(t) = 2\sin(100\pi t)$ µm applied using $G_{e_v}(s)$ given in (14) and $\tilde{G}_{e_v}(s)$ given as

$$\tilde{G}_{e_v}(s) = \frac{0.0015\,s^2 + 1750\,s + 100}{1.0015\,s^2 + 1750\,s + 100} \tag{15}$$

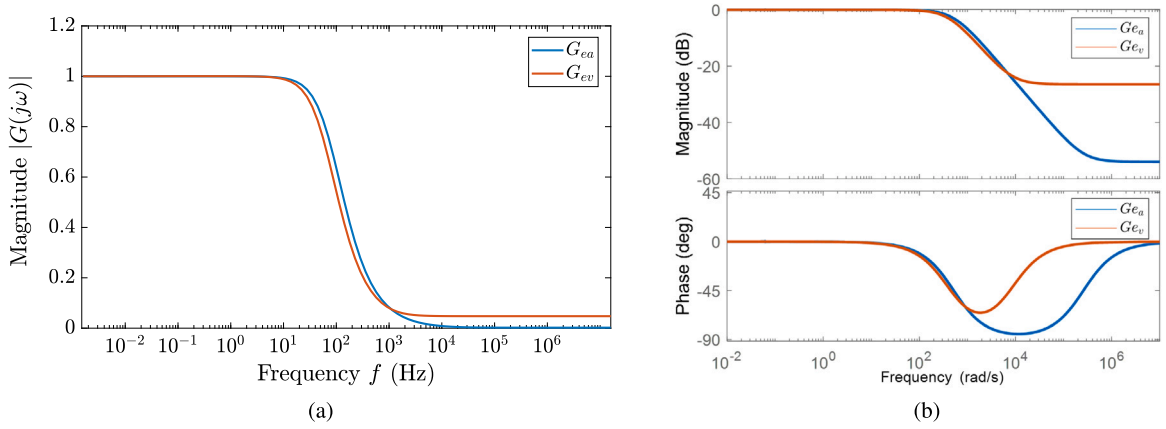

Fig. 6. Response of G_e using the acceleration G_{e_a}, and the velocity G_{e_v} measurements (a) the frequency response function (b) the Bode plot.

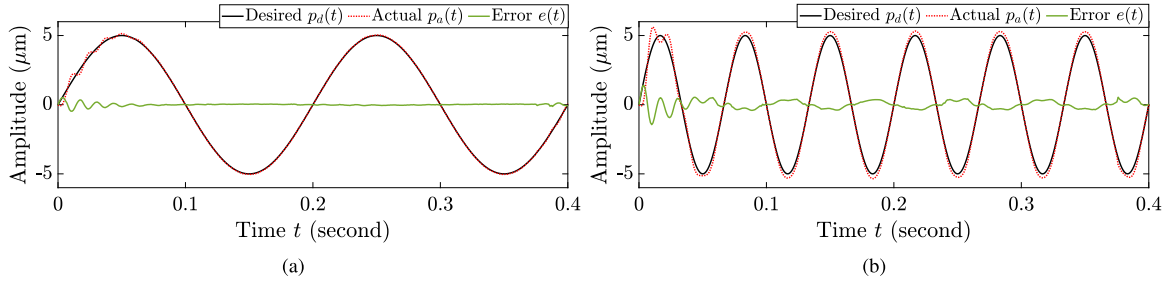

Fig. 7. The experimental results of the piezoelectric-actuated stage time response under $\Sigma_3 \leftrightarrow \Sigma_2$ with $p_d(t) = 5\sin(2\pi f t)$ where (a) $f = 5$ Hz, and (b) $f = 15$ Hz.

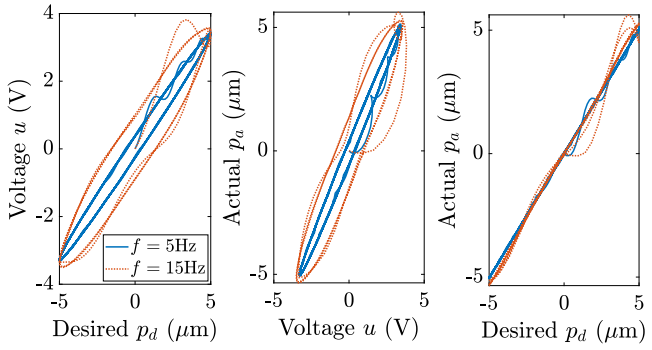

Fig. 8. The input–output characteristic of Σ_3 (left), Σ_2 (middle), and the overall $\Sigma_3 \leftrightarrow \Sigma_2$ compensation (right).

In Fig. 15, the Bode plots of both $G_{e_v}(s)$ and $\tilde{G}_{e_v}(s)$ are depicted with the later has a higher bandwidth based on the newly tuned parameters given in (15). This increase in the bandwidth helps in reducing the tracking error as shown in Fig. 16. This, in fact, motivates us to look into the intertwining of the activator-related transfer function order given in (6), the attainable bandwidth, and the parameters tuning, and the achieved tracking performance, as well be covered in future work.

Welling to test the robustness under high-frequency disturbances, we use a reference signal $p_d(t) = 2\sin(100\pi t)\,\mu$m and a disturbance signal $d(t) = 0.35\sin(2\pi f_d t)$ V with $f_d \in \{10, 50, 750\}$ Hz. Using (15), the tracking errors of the SS stage under the designated disturbances are shown in Fig. 17. Note that $d(t)$ with 10 Hz is inside (15) bandwidth, and $d(t)$ with 50 Hz matches the reference signal $p_d(t)$ frequency, while $d(t)$ with 750 Hz is outside (15) bandwidth. Nevertheless, the robustness of the SS under the aforementioned conditions is clearly maintained under the proposed technique.

5. Application to dual-stage motion system

5.1. Synchronous operation of LS-SS integration

Let y_d, y_a denote the desired and actual positions of the dual-stage system, $\{y_d^{\mathrm{SS}}, y_a^{\mathrm{SS}}\}$ the desired and actual positions of the SS, and y_a^{LS} the actual position of the LS all in the y-direction. Setting $y_d^{\mathrm{SS}} = \boldsymbol{e}_{\mathrm{LS}_y}$, the LS error e_{LS}, the SS error (e_{SS}), and the total tracking error (e_{f_y}) are related such that

$$\boldsymbol{e}_{\mathrm{LS}_y}(t) = y_d(t) - y_a^{\mathrm{LS}}(t) \tag{16}$$

$$\boldsymbol{e}_{\mathrm{SS}_y}(t) = \boldsymbol{e}_{\mathrm{LS}_y}(t) - y_a^{\mathrm{SS}}(t) \tag{17}$$

$$y_a(t) = y_a^{\mathrm{LS}}(t) + y_a^{\mathrm{SS}}(t) \tag{18}$$

$$\boldsymbol{e}_{f_y}(t) = y_d(t) - y_a(t) \equiv \boldsymbol{e}_{\mathrm{SS}_y}(t). \tag{19}$$

where similar relations can be derived for the motion along the x-direction. Therefore, the SS errors e_{SS_x} and e_{SS_y} can be used to assess the performance of the dual-stage system under the herein-proposed approach compared to the RDPI model. Fig. 18 shows the resulting dual-stage positioning system.

5.2. Characteristic of the error

Using $p_d(t) = M\sin(2\pi f_0 t)\,\mu$m with $f_0 \in \{5, 10, 15, 20\}$ Hz and $M \in \{2, 4, 6, 8\}$, the magnitude of the tracking error e_1 under $\Sigma_3 \leftrightarrow \Sigma_2$ interaction can be modeled, for example in the mean-square error sense as

$$\mathrm{MSE}_{e_1} := \mathrm{MSE}_{e_1}(M, \omega_0) = \alpha_0 \omega_0^{\alpha_1}\left(\alpha_2 M^2 + \alpha_3 M + \alpha_4\right) \tag{20}$$

where $\alpha_0 = 0.0009258\pi, \alpha_1 = 1.911, \alpha_2 = 0.1011, \alpha_3 = -0.5863, \alpha_4 = 0.8176$, $\omega_0 = 2\pi f_0 \in \mathrm{BW}(G_e(s))$ denotes the desired operating frequency of $p_d(t)$, and $M \le d_{\max}$ denotes $\max|p_d(t)|$. The resulting error surface is depicted in Fig. 19. Additionally, other parameters can be involved to define MSE_{e_1}. For example, in an LS-SS motion system, (20) can be used

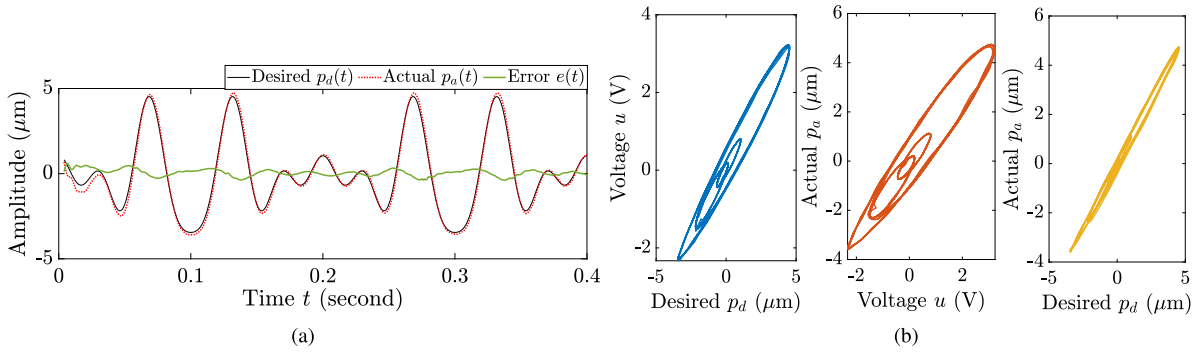

Fig. 9. The (a) piezoelectric-actuated stage time response under $\Sigma_3 \leftrightarrow \Sigma_2$ with mixed-frequency test input signal $p_d(t)$, and (b) the input–output characteristic of Σ_3 (left), Σ_2 (middle), and the overall $\Sigma_3 \leftrightarrow \Sigma_2$ compensation (right).

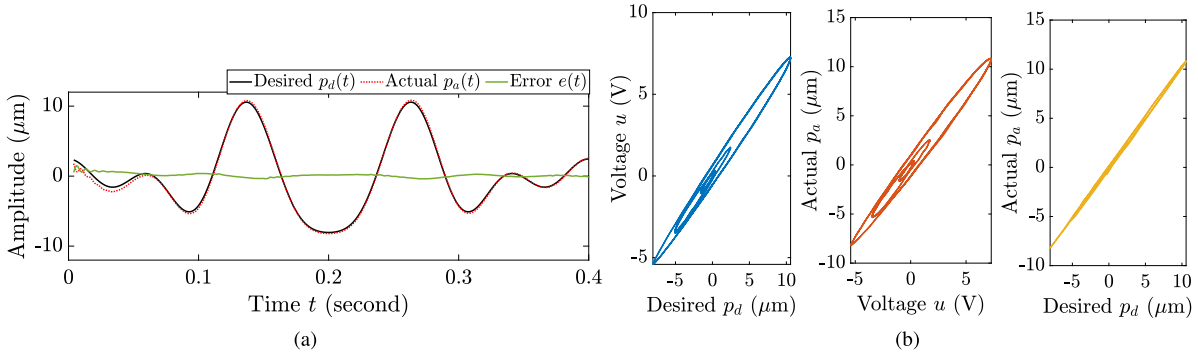

Fig. 10. (a) the time response of the piezoceramic stage under the proposed activator-inhibitor control scheme for desired position $p_d(t)$ presented by (12) with different amplitude and frequencies; and (b) the input–output characteristic of the proposed activator-inhibitor (left), piezoceramic stage (middle), and compensation (right).

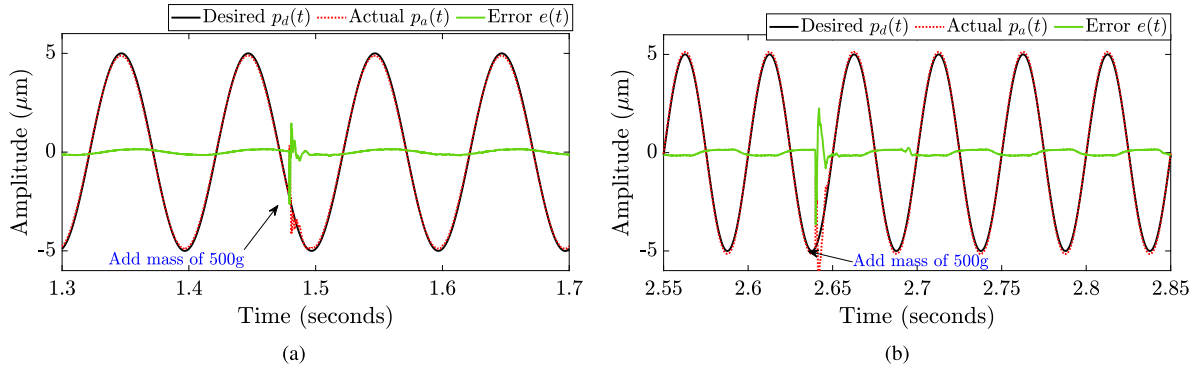

Fig. 11. The experimental results of the piezoelectric-actuated stage time response under $\Sigma_3 \leftrightarrow \Sigma_2$ with $p_d(t) = 5\sin(2\pi f t)$ with load mass $m_l = 500$g where (a) $f = 5$ Hz, and (b) $f = 15$ Hz using $G_{e_v}(s)$ in (14).

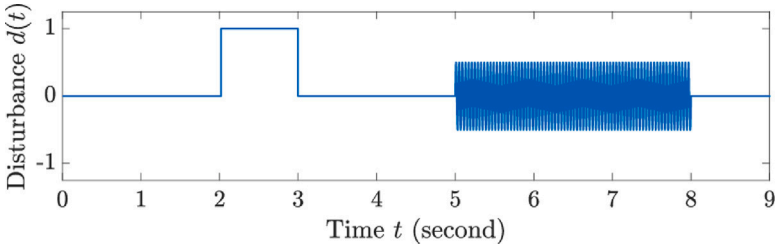

Fig. 12. The disturbance $d(t)$ in (V) added to the control signal $u(t)$ according to Fig. 2.

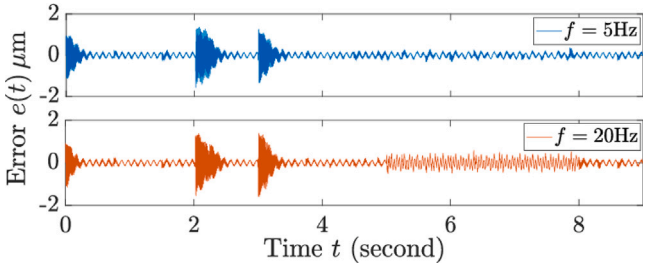

Fig. 13. The error signal $e(t)$ under the disturbance $d(t)$ depicted in Fig. 12 and a desired position $p_d(t)$ with a frequency of 5 Hz (top), and a frequency of 20 Hz (bottom).

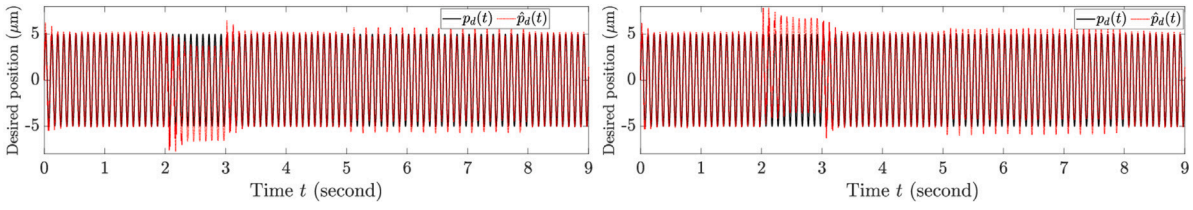

Fig. 14. The modified desired position $\hat{p}_d(t)$ obtained by Σ_3, and the desired position $p_d(t)$ (a) with 5 Hz, and (b) with 20 Hz under the disturbance $d(t)$ shown in Fig. 12.

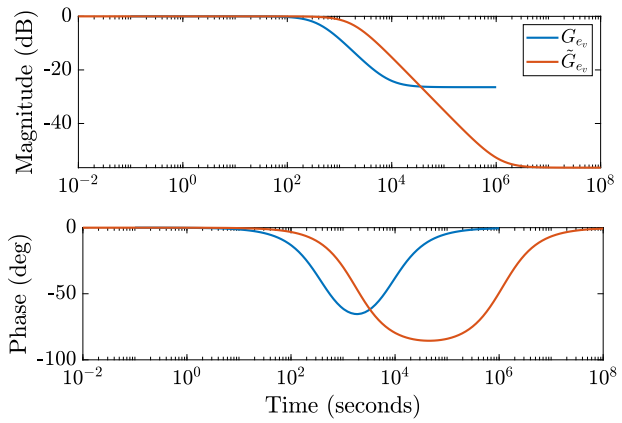

Fig. 15. The Bode response of the activator transfer function G_{e_v} and the re-tuned one $\tilde{G}_{e_v}$ to expand the operation range of frequencies.

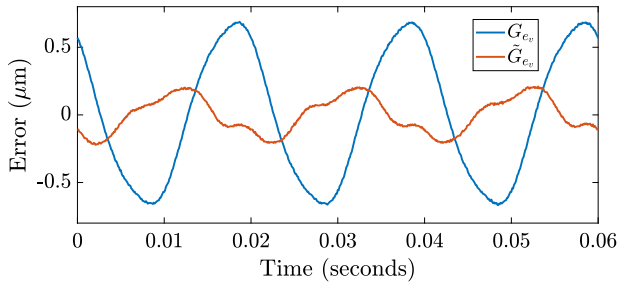

Fig. 16. The tracking error signal $e(t)$ for a desired position $p_d(t) = 2\sin(100\pi t)$ using the activator transfer function G_{e_v} and the re-tuned transfer function $\tilde{G}_{e_v}$.

to define the total tracking error e_{SS} by using $\text{MSE}_{e_1} := \text{MSE}_{SS}(M, \omega_0)$, and $p_d(t) = e_{LS}(t)$. Interestingly, let the frequency-position-dependent statistical model of $e_{LS}(t)$ be given in the mean-square error sense as

$$\text{MSE}_{LS}(x, y, \omega_0) = \sum_{j=1}^{q} \gamma_j(x, y)\, \omega_0^{j-1}, \tag{21}$$

with appropriate coefficients $\gamma_j(x, y)$, the $M = \text{MSE}_{LS}(x, y, \omega_0)$ in (20) yields

$$\text{MSE}_{SS}(\text{MSE}_{LS}, \omega_0) := \text{MSE}_{SS}(x, y, \omega_0). \tag{22}$$

When a fixed value of the overall error $\text{MSE}_{SS}(x, y, \omega_0), \forall\{x, y\}$ is desired, the operational frequency $\omega_0(x, y)$ of the LS can be found and used to define the LS desired trajectories. Accordingly, the error budget and attainable throughput rates of the motion system under any given operational requirements can be determined using (20) and (21) as will be investigated separately.

5.3. Performance assessment

The low-frequency components of e_{SS_y}–for example–can be captured using the error moving average (MA_y) [11]. This metric reflects the wafer scanner ability to expose two images on top of each other, i.e., overlay error. At high frequencies, the moving standard deviation (MSD_y) is used instead mainly to assess the image contrast during exposure [11]. In actual wafer scanners, typical values of a 38-nm half-pitch lithography would be MA $\leq$ 1 nm, and the MSD $\leq$ 7 nm [11] during the constant speed scanning motion. Similarly, in this study, both MA_y and MSD_y are used to assess e_{SS_y} during scanning motion in the y-direction, and they are given as [47]

$$\begin{aligned} \text{MA}_y(t) &= \frac{1}{T}\int_{-\frac{T}{2}}^{\frac{T}{2}} e_{SS_y}(t)\, dt \\ \text{MSD}_y(t) &= \sqrt{\frac{1}{T}\int_{-\frac{T}{2}}^{\frac{T}{2}} \left(e_{SS_y}(t) - \text{MA}_y\right)^2 dt} \end{aligned} \tag{23}$$

where T denotes the time interval of interest, which is usually taken as the constant speed scanning motion [11]. Similarly, MA_x and MSD_x can be used to assess e_{SS_x} during stepping motion in the x-direction—if needed.

5.4. Rate-dependent Prandtl–Ishlinskii (RDPI) feedforward controller for short-stroke

For a given frequency range of interest, and by adopting an input–output perspective, the piezo-actuated SS stage model is captured using the Rate-dependent Prandtl–Ishlinskii (RDPI) hysteresis model that comprises a plurality of n_r weighted rate-dependent play operators

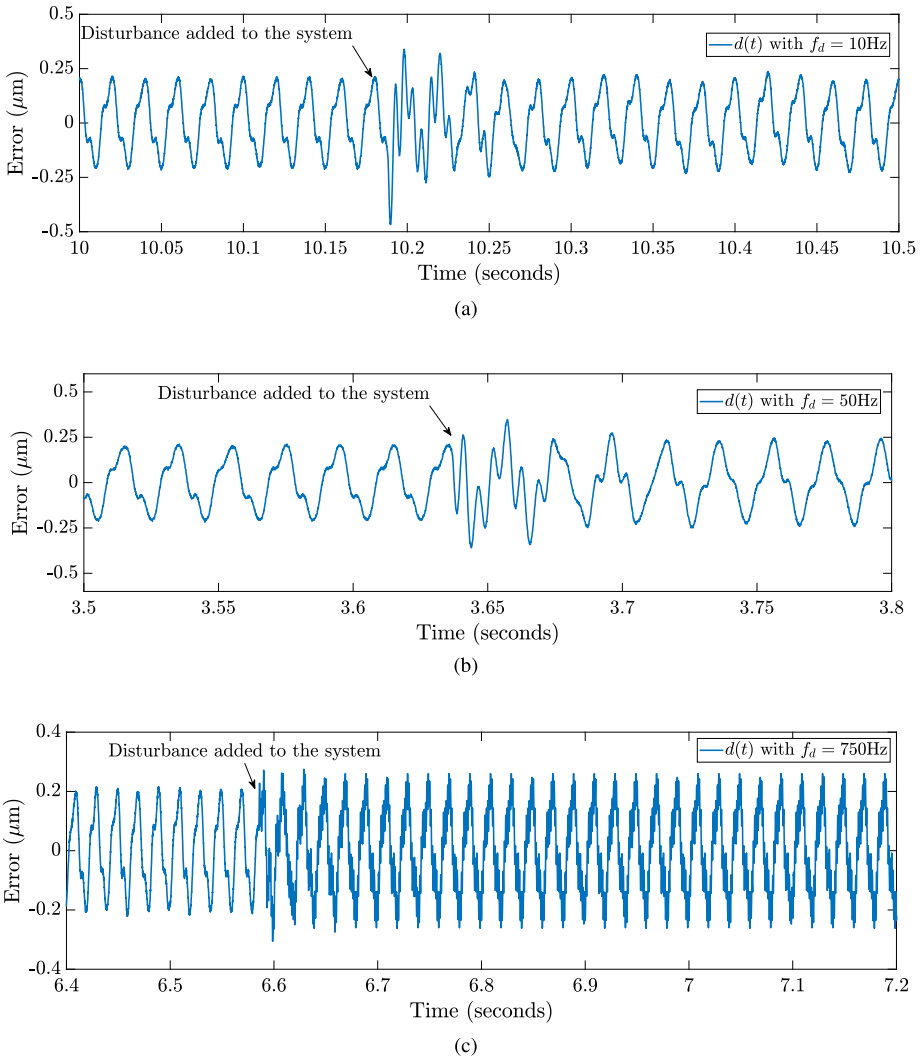

Fig. 17. The tracking error signal $e(t)$ for a desired position $p_d(t) = 2\sin(100\pi t)$ under the sinusoidal disturbance $d(t) = 0.35\sin(2\pi f_d t)$ with a frequency f_d of (a) 10 Hz, (b) 50 Hz, and (c) 750 Hz.

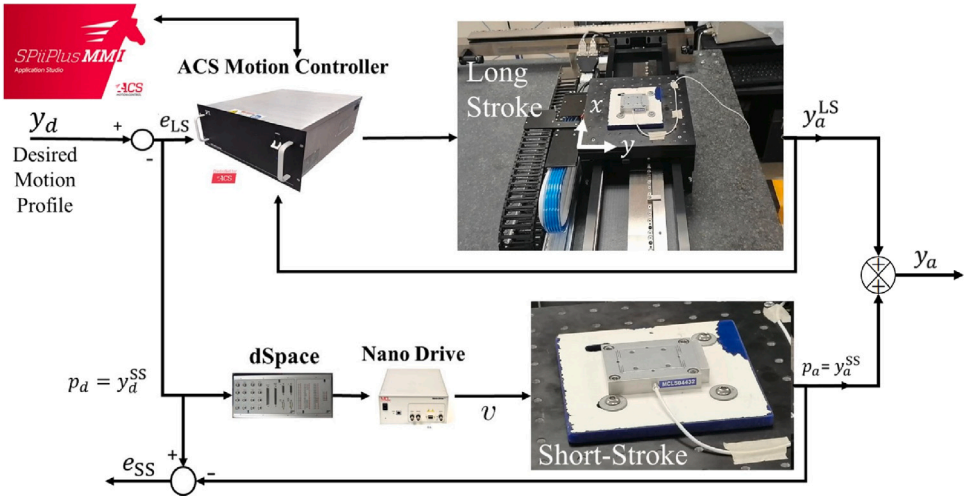

Fig. 18. The LS-SS combined hardware integration showing the used LS-SS acrylic sheet with the SS aligned along the y-axis, i.e. scanning direction.

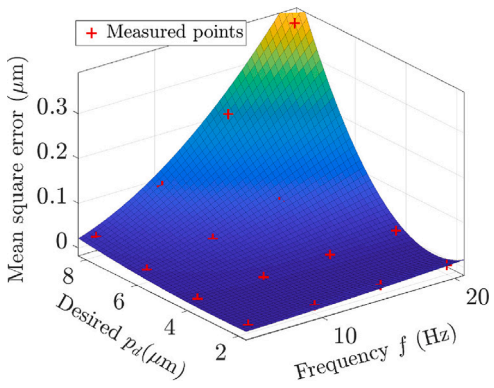

Fig. 19. The $\Sigma_3 \leftrightarrow \Sigma_2$ interaction associated error surface given in the mean-square error sense.

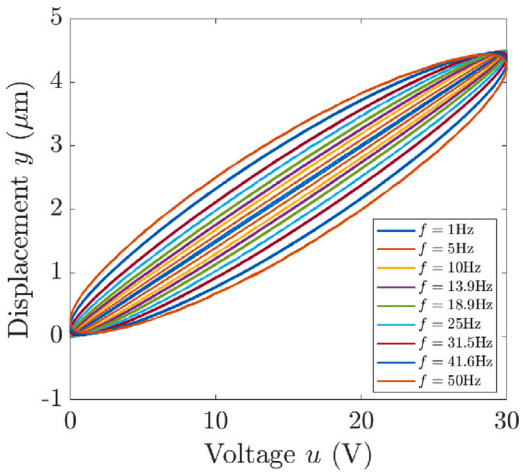

Fig. 20. The voltage-to-displacement hysteresis loops due to a harmonic input voltage with frequency f.

(Γ) with real and absolutely continuous rate-dependent thresholds in order to describe the input–output characteristic of the involved piezo actuators [22,23]. For a monotone input $v(t)$ over the sub-interval $[\tilde{t}_{i-1}, \tilde{t}_i]$ serving as the SS input signal, the output of the RDPI model ($\Psi[v](t)$) in the y-direction–for example–is expressed as [22]

$$y_{SS}(t) = \Psi[v](t) = a_0 v(t) + \sum_{j=1}^{n_r} a_j \Gamma_{\eta_j(t)}[v](t), \tag{24}$$

where $i = 1, 2, \ldots, k$, $0 = \tilde{t}_0 \leq \tilde{t}_1 \leq \cdots \leq \tilde{t}_k = T$, Γ is the rate-dependent play operator with the rate-dependent threshold η_j where $j = 1, 2, \ldots, n_r$, a_0 and a_j are weights to be identified using available SS position y_{SS} measurements. The rate-dependent threshold is a real, absolutely continuous function defined on the interval $[0, T]$ as $0 < \eta_1(t) \leq \eta_2(t) \leq \cdots \leq \eta_{n_r}(t)$. Let the rate-dependent threshold be given as $\eta_j(t) = \sigma_j + \beta|\dot{v}(t)|$, where σ_j and β are positive constants to be identified using the measured data. The operator $\Gamma_{\eta_j(t)}$ over an interval, $t \in [\tilde{t}_{i-1}, \tilde{t}_i)$, is expressed as [22]

$$\Gamma_{\eta_j}[v](t) = \begin{cases} \max\{v(t) - \eta_j, \Gamma_{\eta_j}[v](\tilde{t}_{i-1})\}, & v(t) > v(\tilde{t}_i) \\ \min\{v(t) + \eta_j, \Gamma_{\eta_j}[v](\tilde{t}_{i-1})\}, & v(t) < v(\tilde{t}_i) \\ \Gamma_{\eta_j}[v](\tilde{t}_{i-1}), & v(t) = v(\tilde{t}_i) \end{cases} \tag{25}$$

where $\Gamma_{\eta_j(0)}[v](0) = \max\{v(0) - \eta_j(0), \min\{v(0) + \eta_j(0), 0\}\}$.

To obtain the RDPI model for the SS stage, the measurements y_{SS} are obtained under a harmonic input voltage of $v(t) = 15\sin(2\pi f t) + 15$ V at excitation frequencies of $f_I \equiv f \in \{18.9, 31.5, 41.6\} \subseteq (F_y \bigcup \{1, 10\})$ Hz. Then y_{SS} presents the voltage-to-displacement characteristic as hysteresis loops at different frequencies. Fig. 20 shows these loops between the given testing input $v(t)$ with frequency f_I.

Let $X = \{\beta, \sigma_1, \sigma_2, \ldots, \sigma_{n_r}, a_0, a_1, a_2, \ldots, a_{n_r}\}$ denote the associated parameters of Ψ given in (24). Using y_{SS}, X can be determined by minimizing the cost function given as

$$J(X, \ell, k) = \sum_{\ell=1}^{L} \sum_{k=1}^{N_h} w_p \Big(y_{SS} - \Psi[v](t_k) \Big)^2, \tag{26}$$

where ℓ is the index related to the number of L excitation frequency, w_p is the weight for the ℓ^{th} excitation frequency, and k is the index that refers to the number of N_h data points considered in computing the error for one complete hysteresis loop. The minimization problem is performed using the MATLAB-constrained optimization toolbox subjected to $\beta > 0$, $\sigma_1, \ldots, \sigma_{n_r} \geq 0$. The identified parameters for the RDPI model with $n_r = 5$ are $\beta = 0.0041$, $\sigma_1 = 0.0042$, $\sigma_2 = 0.1031$, $\sigma_3 = 0.1628$, $\sigma_4 = 4.4314$, $\sigma_5 = 6.8909$, $a_0 = 0.0958$, $a_1 = 0.0309$, $a_2 = 0.0159$, $a_3 = 0.0049$, $a_4 = 0.0019$, and $a_5 = 6.7926 \times 10^{-4}$. The identification results of the RDPI model using f_I are depicted in Fig. 21, which shows the ability of the model to capture the piezo-actuated SS stage response in the given range of frequencies. Now, we can present the Prandtl–Ishlinskii-based feedforward controller or compensator. Having the parameters of the RDPI model–representing the SS as in (24)–identified, we seek its inverse (Ψ^{-1}) to realize the feedforward controller based on inversion [22]. Therefore, we may write $y_{SS} = \Psi \circ \Psi^{-1}[e_{LS_y}](t)$, and we have obtained $u(t)$ that minimizes $e_{LS_y} - y_{SS}, \forall t \in [0, T]$. As T goes larger, the involved parameters can be updated online using, e.g. machine learning, as will be investigated in future work. Note that, for mainly repetitive motions, e.g. step-and-scan motion in wafer scanners, $T = 4T_1 + T_2 + D + d$ is fixed, finite, and known a priori [43].

5.5. Comparison results

Fig. 22 illustrates the block diagrams of the LS-SS integration with the two proposed control approaches. Starting with the desired position signals $y_d(t)$ and $x_d(t)$ depicted in Fig. 5, the associated frequency contents can be determined using fast Fourier transform (FFT), and consequently, the bandwidth of interest can be determined as pictured in Fig. 23. Accordingly, $G_e(s)$ in (6) can be designed, and its bandwidth (BW$\{G_e(s)\}$) can be assigned. For example, as depicted in Fig. 23, the frequency contents of both e_{LS_x} and e_{LS_y} have a significant contribution below 20 Hz. According to Fig. 2, both e_{LS_x} and e_{LS_y} can serve as the input to Σ_2 once the available SS stage is aligned in their designated directions, i.e., $p_d(t) \equiv e_{LS_x}(t)$ or $p_d(t) \equiv e_{LS_y}(t)$, based on the LS-SS configuration depicted in Fig. 22(a).

Utilizing the block diagrams of the LS-SS integration shown in Fig. 22, when no disturbance is active, i.e., $d = 0$, both the model-free $\Sigma_3 \leftrightarrow \Sigma_2$ interaction and the model-based RDPI model resulted in almost a similar tracking error considering the motion along the x-direction as depicted in Fig. 24. However, when $d \neq 0$, the model-free $\Sigma_3 \leftrightarrow \Sigma_2$ interaction outperforms the model-based RDPI model due to the former's awareness of the actual SS response through the available feedback measurements. Similar results can be deduced about the tracking error along the y-direction as can be seen from Fig. 25. The disturbance d is imitated using a pulse of amplitude 0.3 V, $\forall t \in [4, 5]$ s, where the piezo amplifier internally provides a gain of 10 to this applied disturbance. The effects on the desired signal in the x-direction can be seen from Fig. 26, where interestingly the control signal $r(t)$ is not affected by $d(t)$. Recalling Fig. 2, Σ_3 changes the desired signal $q_1 \equiv p_d$ such that the resulting control signal $r(t) = u(t) + d(t)$ is not affected by $d(t)$. Note that this will not be the case when the disturbance appears at the output side, i.e., p_a. This case will be examined in a separate study.

Using (23) with T covering the whole range of motion, i.e., about 4 s, the performance of the dual-stage system under $\Sigma_3 \leftrightarrow \Sigma_2$ interaction compared to the RDPI model is assessed when $d(t) = 0$. As

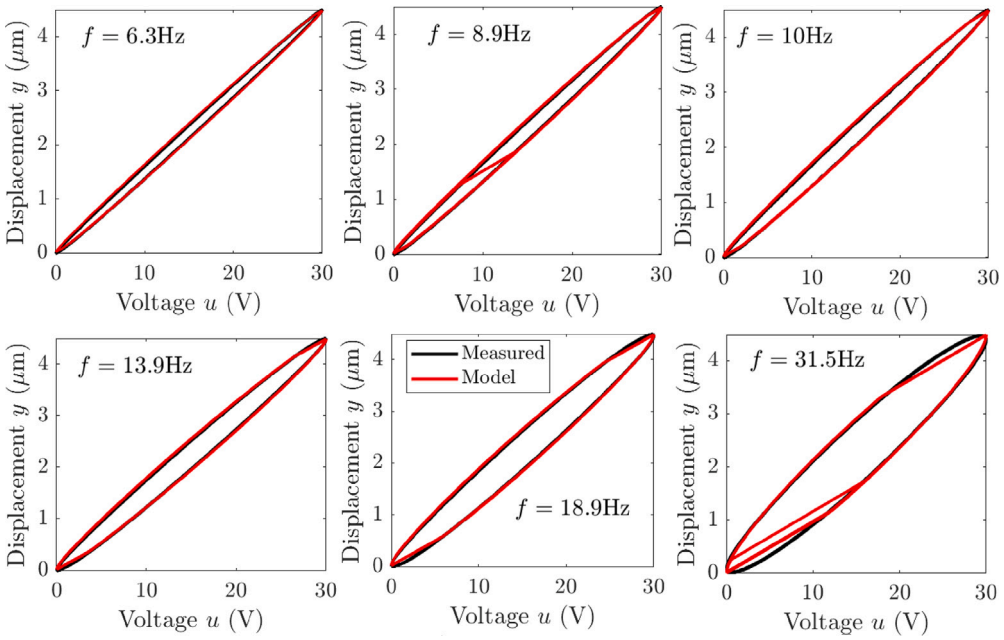

Fig. 21. The comparison between the measured hysteresis loops and the obtained loops using the RDPI model with $n_r = 5$.

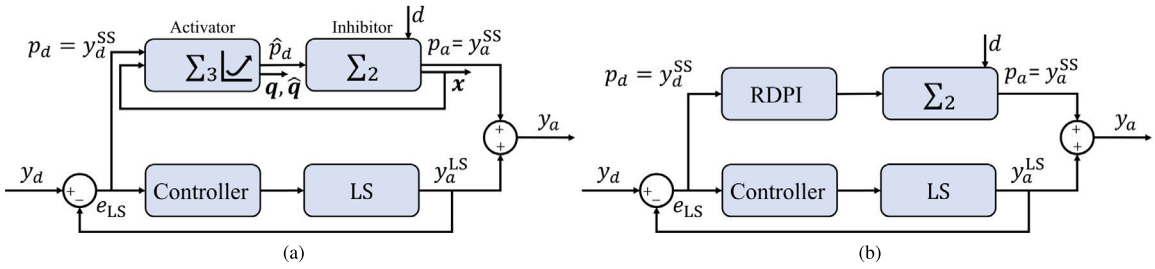

Fig. 22. The block diagram of the LS-SS integration under (a) $\Sigma_3 \leftrightarrow \Sigma_2$ interaction, and (b) RDPI model, in the y-direction, where Σ_2 denotes the SS piezo-actuated stage.

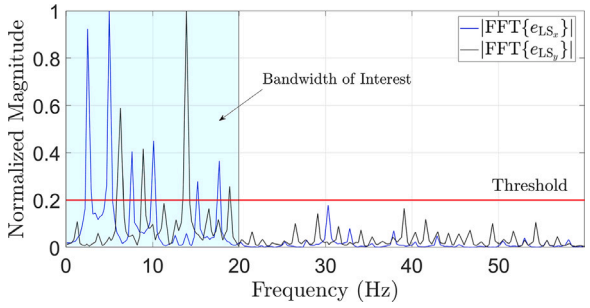

Fig. 23. Single-sided amplitude spectrum of e_{LS_x} and e_{LS_y} of the 10 dies scanning profile.

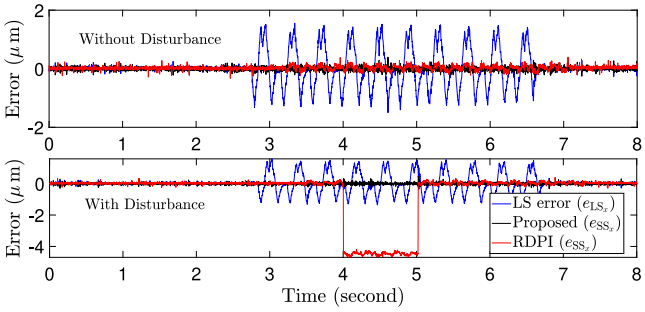

Fig. 24. The tracking errors of the LS-SS system along x direction with and without disturbance d.

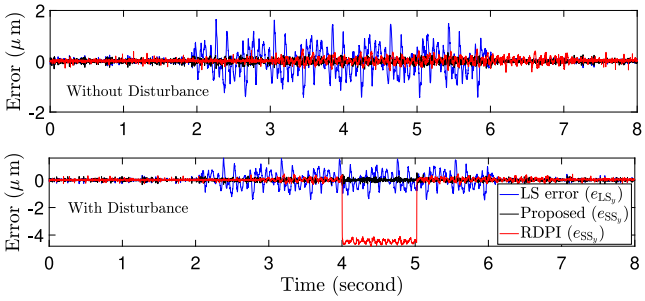

Fig. 25. The tracking errors of the LS-SS system along y direction with and without disturbance d.

shown in Fig. 27, $\Sigma_3 \leftrightarrow \Sigma_2$ interaction outperforms the RDPI model at low frequencies as captured by the MA metric, while both almost do nothing to e_{LS_x} and e_{LS_y} at higher frequencies as captured by the MSD metric. Only a sampling rate of 1 ms was used in this study. The effect of using a higher sampling rate and higher value of n in (6) on specifically the MSD performance metric will be investigated in future work.

6. Conclusion

This paper introduces a model-free control approach for the short-stroke stage, which is driven by a piezoelectric actuator. The proposed approach employs an activator-inhibitor scheme, dynamically mitigating the nonlinearities in the short-stroke stage without relying on

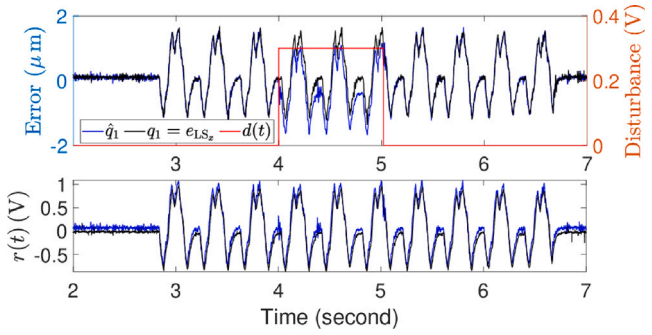

Fig. 26. The (top) SS modified tracking error $\hat{q}_1$ (blue) in the x-direction when $d \neq 0$, and (bottom) the corresponding control input, $r(t) = u(t) + d(t)$ both compared to the case when $d = 0$ (black).

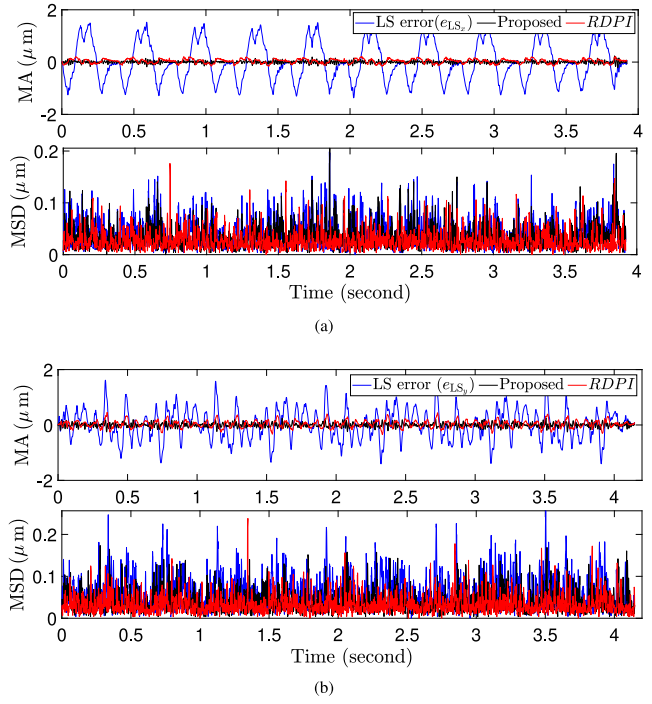

Fig. 27. The MA and MSD tracking error performance metrics of the LS-SS system along (a) x, and (b) y directions, without disturbance, i.e., $d = 0$.

modeling or identifying its dynamics. The proposed approach is an observer that shapes the desired input signal (tracking error) to meet the dynamic requirements of the fine stage, even in the presence of disturbances. The proposed activator-inhibitor approach is implemented as a controller to enhance the tracking performance of the piezoelectric-actuated stage. Experimental testing of the proposed approach is conducted for the piezoelectric-actuated stage under desired positions with varying amplitudes and frequencies. The experimental results demonstrate the capability of the proposed control approach to reduce tracking error and enhance performance. Additionally, it is observed that the input–output characteristic of the activator-inhibitor scheme acts as an inverse of the dynamic model. Moreover, the proposed activator-inhibitor scheme exhibits robustness in achieving tracking performance in the presence of external disturbances. For practical applications, we integrate a dual-stage motion system that simulates wafer scanners by employing the uni-axial piezoelectric-actuated stage under the proposed technique, within an existing long-stroke motion system. A comparison with the Prandtl–Ishlinskii inverse model underscores the advantages of our proposed model-free activator-inhibitor control. Its performance surpasses that of the model-based method, particularly at low frequencies of the command signal, as indicated by the moving average performance metric. Our future endeavors will focus on refining the performance of the proposed activator-inhibitor control at higher frequencies guided by the moving standard deviation performance metric.

CRediT authorship contribution statement

Yazan M. Al-Rawashdeh: Methodology, Investigation, Formal analysis, Data curation, Conceptualization. **Mohammad Al Saaideh:** Methodology, Formal analysis, Data curation, Conceptualization. **Marcel F. Heertjes:** Project administration, Methodology, Investigation, Conceptualization. **Tom Oomen:** Writing – original draft, Project administration, Methodology, Investigation, Conceptualization. **Mohammad Al Janaideh:** Supervision, Resources, Funding acquisition, Conceptualization.

Declaration of competing interest

The authors declare that they have no known competing financial interests or personal relationships that could have appeared to influence the work reported in this paper.

Data availability

No data was used for the research described in the article.

Acknowledgement

This work was supported in part by the Natural Sciences and Engineering Research Council of Canada (NSERC) by an Alliance International Catalyst grant and in part by the Canada Foundation for Innovation (CFI).

References

[1] Du X, Shen D, Huang P, Zhu L, Zhu Z. Dual-stage fast tool servo cascading a primary normal-stressed electromagnetic stage with a secondary piezo-actuated stage. Precis Eng 2023;80:171–9.
[2] Mitrovic A, Nagel W, Leang K, Clayton G. Closed-loop range-based control of dual-stage nanopositioning systems. IEEE/ASME Trans Mechatronics 2020;26:1412–21.
[3] Guo D, Nagel W, Clayton G, Leang K. Spatial-temporal trajectory redesign for dual-stage nanopositioning systems with application in AFM. IEEE/ASME Trans Mechatronics 2020;25:558–69.
[4] Barros C, Butler H, van de Wijdeven J, Tóth R. On feedforward control of piezoelectric dual-stage actuator systems. In: 60th IEEE conference on decision and control. CDC, IEEE; 2021, p. 5588–94.
[5] Jain A. Multibody graph transformations and analysis: part I: tree topology systems. Nonlinear Dyn 2012;67:2779–97.
[6] Divijesh P, Rao M, Rao R, Jain N, Prabhu P. Implementation of structurally prestressed piezo actuator based active vibration isolation system for micro milling. In: Materials Today: Proceedings. 92, Elsevier; 2023, p. 182–8.
[7] Sato K, Hisamatsu R, Akamatsu K. Controller design for high-speed, ultra-precision positioning of a linear motion stage on a vibrating machine base stage control on a vibrating base. Precis Eng 2023;80:10–9.
[8] Behera D, Chizari S, Shaw LA, Porter M, Hensleigh R, Xu Z, et al. Current challenges and potential directions towards precision microscale additive manufacturing–Part IV: Future perspectives. Precis Eng 2021;68:197–205.
[9] Heertjes MF, Butler H, Dirkx N, van der Meulen S, Ahlawat R, O'Brien K, et al. Control of wafer scanners: Methods and developments. In: 2020 American control conference. ACC, IEEE; 2020, p. 3686–703.
[10] Heertjes M, Van der Velden B, Oomen T. Constrained iterative feedback tuning for robust control of a wafer stage system. IEEE Trans Control Syst Technol 2016;24(1):56–66.
[11] Butler H. Position control in lithographic equipment. IEEE Control Syst Mag 2011;31(5):28–47.
[12] Mack C. Fundamental principles of optical lithography: The science of microfabrication. Hoboken, NJ, USA: John Wiley & Sons; 2008.
[13] Chen Z, Shi J, Zhu S, Zhong X, Zhang X. Design and testing of a damped piezo-driven decoupled xyz stage. In: 2021 IEEE international conference on robotics and automation. ICRA, IEEE; 2021, p. 6986–91.
[14] Salton AT, Fu M, Flores JV, Zheng J. High precision over long range: A macro–micro approach to quantized positioning systems. IEEE Trans Control Syst Technol 2020;29(6):2406–15.

[15] Woronko A, Huang J, Altintas Y. Piezoelectric tool actuator for precision machining on conventional CNC turning centers. Precis Eng 2003;27(4):335–45.
[16] Fung R-F, Hsu Y-L, Huang M-S. System identification of a dual-stage XY precision positioning table. Precis Eng 2009;33(1):71–80.
[17] Mohith S, Upadhya AR, Navin KP, Kulkarni S, Rao M. Recent trends in piezoelectric actuators for precision motion and their applications: A review. Smart Mater Struct 2020;30(1):013002.
[18] Sabarianand D, Karthikeyan P, Muthuramalingam T. A review on control strategies for compensation of hysteresis and creep on piezoelectric actuators based micro systems. Mech Syst Signal Process 2020;140:106634.
[19] Singh A, Libby T, Fuller SB. Rapid inertial reorientation of an aerial insect-sized robot using a piezo-actuated tail. In: 2019 international conference on robotics and automation. ICRA, IEEE; 2019, p. 4154–60.
[20] Shi B, Shi R, Wang F. Design of an adaptive feedforward/feedback combined control for piezoelectric actuated micro positioning stage. Precis Eng 2022;78:199–205.
[21] Ling J, Feng Z, Chen L, Zhu Y, Pan Y. Neural network-based iterative learning control of a piezo-driven nanopositioning stage. Precis Eng 2023;81:112–23.
[22] Al Janaideh M, Krejčí P. Inverse rate-dependent Prandtl–Ishlinskii model for feedforward compensation of hysteresis in a piezomicropositioning actuator. IEEE/ASME Trans Mechatron 2012;18(5):1498–507.
[23] Al Janaideh M, Aljanaideh O. Further results on open-loop compensation of rate-dependent hysteresis in a magnetostrictive actuator with the Prandtl-Ishlinskii model. Mech Syst Signal Process 2018;104:835–50.
[24] Strijbosch N, Tiels K, Oomen T. Memory-element-based hysteresis: Identification and compensation of a piezoelectric actuator. IEEE Trans Control Syst Technol 2023;31(6):2863–70.
[25] Strijbosch N, Tiels K, Oomen T. Hysteresis feedforward compensation: A direct tuning approach using hybrid-MEM-elements. IEEE Control Syst Lett 2021;6:1070–5.
[26] Flores G, Rakotondrabe M. Finite-time stabilization of the generalized Bouc–Wen model for piezoelectric systems. IEEE Control Syst Lett 2022;7:97–102.
[27] Xu Q, Li Y. Dahl model-based hysteresis compensation and precise positioning control of an XY parallel micromanipulator with piezoelectric actuation. 132, (4):2010, 041011.
[28] Zhang Z, Zhang D, Zheng H, Huang T, Xie Y. Identification of a precision motion stage based on the Hammerstein-Wiener model. In: 2019 Chinese control conference. CCC, IEEE; 2019, p. 1637–42.
[29] Wang J, Xu Q. Precision tracking control of piezoelectric-driven motion system based on enhanced ADRC. In: 2020 39th Chinese control conference. CCC, IEEE; 2020, p. 2626–30.
[30] Kasemsinsup Y, Heertjes M, Butler H, Weiland S. Exact plant inversion of flexible motion systems with a time-varying state-to-output map. In: 2016 European Control Conference. ECC, IEEE; 2016, p. 2483–8.
[31] Dewey J, Leang K, Devasia S. Experimental and theoretical results in output-trajectory redesign for flexible structures. In: Proceesings of 35th IEEE conference on decision and control. CDC, IEEE; 1998, p. 4210–5.
[32] Rodriguez-Fortun JM, Rotella F, Alfonso J, Carrillo FJ, Orus J. Model-free control of a 3-DOF piezoelectric nanopositioning platform. In: 52nd IEEE conference on decision and control. CDC, IEEE; 2013, p. 342–7.
[33] Naghdi M, Izadi I, Alem SF. Sampled-data model-free adaptive sliding mode control for piezoelectric actuators subject to time delay. IFAC-PapersOnLine 2023;56(2):2468–73.
[34] Lee J, Laffranchi M, Kashiri N, Tsagarakis NG, Caldwell DG. Model-free force tracking control of piezoelectric actuators: application to variable damping actuator. In: 2014 IEEE international conference on robotics and automation. ICRA, IEEE; 2014, p. 2283–9.
[35] Al-Rawashdeh Y, Al Janaideh M, Heertjes M. On characterization of a generic lithography machine in a multi-directional space. Mech Mach Theory 2022;170:104638.
[36] Al Janaideh M, Bernstein DS. Adaptive control of uncertain Hammerstein systems with hysteretic nonlinearities. In: 53rd IEEE conference on decision and control. IEEE; 2014, p. 545–50.
[37] Aljanaideh KF, Al Janaideh M, Rakotondrabe M, Al Saaideh M, Almomani AM, Bani Hani MA, et al. Identification of a class of precision motion systems with uncertain hysteretic nonlinearities. Internat J Control 2023;96(8):1971–88.
[38] Chowdhury D, Al-Nadawi YK, Tan X. Hysteresis compensation using extended high-gain observer and dynamic inversion. In: Dynamic systems and control conference. DSCC, 51906, American Society of Mechanical Engineers; 2018, V002T24A005.
[39] Khalil HK, Praly L. High-gain observers in nonlinear feedback control. Int. J. Robust Nonlinear Control. 2014;24(6):993–1015.
[40] Xie Y, Tan Y, Dong R. Nonlinear modeling and decoupling control of XY micropositioning stages with piezoelectric actuators. IEEE/ASME Trans Mechatronics 2012;18(3):821–32.
[41] Jan C, Hwang C-L. Robust control design for a piezoelectric actuator system with dominant hysteresis. In: 2000 26th annual conference of the IEEE industrial electronics society. IECON 2000. 2000 IEEE international conference on industrial electronics, control and instrumentation. 21st century technologies, vol. 3. IEEE; 2000, p. 1515–20.
[42] Al-Rawashdeh YM, Al Saaideh M, Boker AM, Eldardiry H, Heertjes MF, Al Janaideh M. Trajectory generation using activator-inhibitor systems. In: 2023 62nd IEEE conference on decision and control. CDC, IEEE; 2023, p. 8857–63.
[43] Al-Rawashdeh Y, Al Janaideh M, Heertjes M. Kinodynamic generation of wafer scanners trajectories used in semiconductor manufacturing. IEEE Trans Autom Sci Eng 2022;20:718–32.
[44] Khalil HK. Nonlinear systems, vol. 115. 3rd ed. Patience Hall; 2002.
[45] Al-Rawashdeh Y, Al Janaideh M, Heertjes M. On step-and-scan trajectories used in wafer scanners in semiconductor manufacturing. In: 2021 IEEE/RSJ International Conference on Intelligent Robots and Systems (IROS). 2021, p. 7580–6.
[46] Al-Rawashdeh Y, Al Janaideh M, Heertjes M. Kinodynamic generation of wafer scanners trajectories used in semiconductor manufacturing. IEEE Trans Autom Sci Eng 2023;20(1):718–32.
[47] Heertjes M. Data-based motion control of wafer scanners. IFAC-PapersOnLine 2016;49:1–12.

Yazan M. Al-Rawashdeh received his B.Sc. degree in Mechatronics Engineering from The University of Jordan (UJ), Amman, Jordan, in 2006, and his M.Sc. and Ph.D. in Systems and Control Engineering from King Fahd University of Petroleum and Minerals (KFUPM), Dhahran, Saudi Arabia, in 2014 and 2018, respectively. Recently, he joined the Electrical Engineering Department at Al-Zaytoonah University of Jordan, Amman, Jordan as an assistant professor. His current research interests are control of multi-agent systems and semiconductor manufacturing.

Mohammad Al Saaideh received his B.Sc. and M.Sc. degrees in Electrical Engineering from the University of Jordan, Jordan, in 2013 and 2020, respectively, and his Ph.D. degree in Electrical Engineering from Memorial University, Canada, in 2024. He is a postdoctoral researcher with the Department of Electrical and Computer Engineering at the Memorial University of Newfoundland, St. John's, NL, Canada. He received the "Fellow of the School of Graduate Studies" for the Year 2022-2023 in recognition of outstanding academic achievement throughout a Ph.D. program. His research interests include analyzing and controlling nonlinear systems, designing, and controlling a reluctance actuator for a wafer scanner system in semiconductor manufacturing machines, and controlling precision motion systems with uncertain hysteresis nonlinearities.

Marcel Heertjes received the M.Sc. and Ph.D. degrees from the Eindhoven University of Technology, Eindhoven, The Netherlands, in 1995 and 1999, respectively. After being with the Philips Center for Industrial Technology from 2000–2005, he joined ASML in 2006 where he currently is appointed Sr. principle mechatronics architect. He was a recipient of the IEEE Control Systems Technology Award 2015 for variable gain control and its applications to wafer scanners and the 2023 Automatica Paper Prize on projection-based integrators for improved motion control, among others. In 2019, he was appointed (part-time) full Professor on Industrial Nonlinear Control for High-Precision Systems at Eindhoven University of Technology. He acts as an Associate Editor for IFAC Mechatronics since 2016.

Tom Oomen is full professor with the Department of Mechanical Engineering at the Eindhoven University of Technology. He is also a part-time full professor with the Delft University of Technology. He received the M.Sc. degree (cum laude) and Ph.D. degree from the Eindhoven University of Technology, Eindhoven, The Netherlands. He held visiting positions at KTH, Stockholm, Sweden, and at The University of Newcastle, Australia. He is a recipient of the 7th Grand Nagamori Award, the Corus Young Talent Graduation Award, the IFAC 2019 TC 4.2 Mechatronics Young Research Award, the 2015 IEEE Transactions on Control Systems Technology Outstanding Paper Award, the 2017 IFAC Mechatronics Best Paper Award, the 2019 IEEJ Journal of Industry Applications Best Paper Award, and recipient of a Veni and Vidi personal grant. He is currently a Senior Editor of IEEE Control Systems Letters (L-CSS) and Associate Editor of IFAC Mechatronics, and he has served on the editorial boards of the IEEE Control Systems Letters (L-CSS) and IEEE Transactions on Control Systems Technology. He has also been vice-chair for IFAC TC 4.2 and a member of the Eindhoven Young Academy of Engineering. His research interests are in the field of data-driven modeling, learning, and control, with applications in precision mechatronics.

Mohammad Al Janaideh received the M.A.Sc. and Ph.D. degrees in mechanical engineering (mechatronics and control) from Concordia University, Montréal, QC, Canada. He was a Postdoctoral Fellow with the Department of Electrical and Computer Engineering, University of Toronto, Toronto, ON, Canada, and the Department of Aerospace Engineering, University of Michigan, Ann Arbor, MI, USA. He was also a Senior Mechatronics Engineer with ASML, Wilton, CT, USA. He is currently with the School of Engineering, University of Guelph, Guelph, ON. His research interests include design and control of micro- and nanopositioning systems, fault detection and mitigation of connected autonomous robotics networks, design and control of precision motion stages for semiconductor manufacturing machines, and control of systems with uncertain hysteresis nonlinearities. Dr. Al Janaideh is a Technical Editor for IEEE Transactions on Mechatronics, IEEE Conference of Decision and Control, and American Control Conference.